

Effect of Al and Nb Doping on the Electrochemical Characteristics of Garnet-type $\text{Li}_7\text{La}_3\text{Zr}_2\text{O}_{12}$ Solid Electrolytes

Ahmed Tarif and Chan-Jin Park[†]

Department of Materials Science and Engineering, Chonnam National University, 77, Yongbong-ro, Buk-gu, Gwangju 61186, Korea
(Received November 10, 2023; Revised December 06, 2023; Accepted December 07, 2023)

In this study, we synthesized and characterized garnet-type $\text{Li}_{7-x}\text{Al}_x\text{La}_3\text{Zr}_{2-(5/4)y}\text{Nb}_y\text{O}_{12}$ (LALZN) solid electrolytes for all-solid-state battery applications. Our novel approach focused on enhancing ionic conductivity, which is crucial for battery efficiency. A systematic examination found that co-doping with Al and Nb significantly improved this conductivity. Al^{3+} and Nb^{5+} ions were incorporated at Li^+ and Zr^{4+} sites, respectively. This doping resulted in LALZN electrolytes with optimized properties, most notably enhanced ionic conductivity. An optimized mixture with 0.25 mol each of Al and Nb dopants achieved a peak conductivity of $1.32 \times 10^{-4} \text{ S cm}^{-1}$. We fabricated symmetric cells using these electrolytes and observed excellent charge-discharge profiles and remarkable cycling longevity, demonstrating the potential for long-term application in battery systems. The garnet-type LALZN solid electrolytes, with their high ionic conductivity and stability, show great potential for enhancing the performance of all-solid-state batteries. This study not only advances the understanding of effective doping strategies but also underscores the practical applicability of the LALZN system in modern energy storage solutions.

Keywords: Solid electrolyte, Garnet, Doping, Ionic conductivity, Solid-state batteries

1. Introduction

Rechargeable lithium-ion batteries (LIBs) have emerged as a leading electrochemical power source, addressing contemporary global energy challenges. They serve as essential energy reservoirs for various applications, including electric vehicles (EVs), mobile phones, laptops, IC cards, and other portable electronics, as well as stationary power storage, owing to their high energy density, extended cycle life, and environmental sustainability [1-3]. However, the use of organic liquid electrolytes poses safety concerns due to their flammability and potential toxicity, limiting the broader applicability of LIBs [4,5]. Therefore, there is a pressing need to explore alternative electrolyte materials to enhance safety. In this context, the development of all-solid-state lithium-ion batteries (ASSLIBs) using solid electrolytes as substitutes for liquid counterparts represents a promising avenue for ensuring improved safety.

ASSLIBs with solid electrolytes offer solutions to safety

concerns related to the flammability and leakage of batteries using liquid electrolytes. Owing to the high theoretical capacity and low negative electrochemical potential of lithium [6-8], coupled with the reduced thickness and expanded operating potential window of solid electrolytes [9,10], ASSLIBs exhibit enhanced energy density. Various inorganic solid electrolytes have been studied for use in ASSLIBs, encompassing sulfides [11-13], nitrides [14], phosphates [15,16], and oxides [17]. However, perovskite-type oxides and NASICON-type phosphates exhibit instability in the presence of metallic Li [10,18]. Similarly, LISICON-type sulfides demonstrate instability with Li and release H_2S upon exposure to moisture [19]. Additionally, nitride-based electrolytes can form an insulating layer when in contact with Li metal [14].

Among the various electrolytes, garnet-type $\text{Li}_7\text{La}_3\text{Zr}_2\text{O}_{12}$ (LLZO) oxide solid electrolytes have garnered significant attention due to their high ionic conductivity ($\sim 10^{-4} \text{ S cm}^{-1}$) and an expansive electrochemical potential window exceeding 5 V, along with robust stability against Li metal [17,20,21]. Murugan first synthesized LLZO in 2007 and characterized its properties as a rapid Li-ion conductor

[†]Corresponding author: parkcj@jnu.ac.kr

Ahmed Tarif: Grade student, Chan-Jin Park: Professor

[17]. Notably, two distinct phases have been identified in LLZO: tetragonal and cubic [22-24]. Given that the structure of LLZO profoundly influences Li-ion distribution and migration pathways, the cubic phase of LLZO offers ionic conductivity that is two orders of magnitude higher than its tetragonal counterpart [22, 24,25]. However, pristine LLZO predominantly exhibits the tetragonal phase at room temperature and struggles to stabilize in the cubic phase. Consequently, modifications to LLZO are essential to stabilize the cubic phase and enhance ionic conductivity.

Recently, significant advancements have been made in enhancing the performance and ionic conductivity of LLZO through doping modifications. In this context, several dopants have been identified as effective in boosting ionic conductivity. For instance, Al^{3+} [26] and Ga^{3+} [27-31] have been doped at Li^+ sites, while Te^{6+} [32], Sb^{5+} [33], W^{6+} [34], Ta^{5+} [35], and Nb^{5+} [36] have been introduced at Zr^{4+} sites. Doping serves to amplify the ionic conductivity by inducing vacancies, disordering Li-ion distribution, and stabilizing the cubic phase, while simultaneously lowering the sintering temperature. Furthermore, for the dual purpose of reducing the sintering temperature and augmenting conductivity, cations with larger radii such as Sr^{2+} or Ce^{4+} can be doped at La^{3+} sites [37,38]. Another pivotal consideration is the role of grain boundaries in determining the microstructure, which in turn affects the quality of the LLZO surface. "A dense microstructure is instrumental in enhancing ionic conductivity, as it reduces grain boundary resistance and mitigates dendrite formation during lithium deposition. Consequently, the selection of appropriate doping sites is paramount in optimizing the properties and ionic conductivities of LLZO electrolytes.

It is imperative to explore the simultaneous substitution of Li^+ or La^{3+} and Zr^{4+} sites with appropriate dopants during the synthesis of LLZO solid electrolytes. The dual doping technique offers potential to enhance phase structure and conductivity, benefiting both fabrication and application. Takahiko Asaoka demonstrated that only Sr or Ca can be doped into La in Nb-LLZO (where Nb substituted Zr), resulting in the formation of a cubic garnet structure. However, doping with Mg or Ba in the La site introduced impurity phases [39]. In contrast, prior studies have employed dual doping strategies, such as Ta

substituting Zr [40], Sb replacing Zr [41] in Al-LLZO (with Al doped into Li), and combinations of Ga in Li and Sc in Zr [42], to augment ionic conductivity. These dual doping approaches have been shown to induce desirable properties, including the formation and stabilization of the cubic phase, reduction in sintering temperature, denser morphologies, and overall improved ionic conductivity.

Given this context, we opted for Al and Nb to achieve a dual doping effect in LLZO. A double-doped LLZO was synthesized, with varying concentrations of both Al and Nb, aiming to enhance both bulk and grain boundary conductivities. This effort yielded an optimized composition of $\text{Li}_{6.25}\text{Al}_{0.25}\text{La}_3\text{Zr}_{1.69}\text{Nb}_{0.25}\text{O}_{12}$ (LALZN), achieving an ionic conductivity nearing the order of $10^{-4} \text{ S cm}^{-1}$, making it suitable for Li-ion batteries. Comprehensive electrochemical analyses were performed on LALZN ceramics. These were then employed as the primary solid electrolytes, substituting traditional liquid electrolytes in ASSLIBs.

2. Experimental Procedure

2.1. Material synthesis

Li_2CO_3 (Alfa Aesar, 99%), La_2O_3 (Alfa Aesar, 99.999%), ZrO_2 (Alfa Aesar, 99.7%), Al_2O_3 (Hanawa Chemical, pure grade), and Nb_2O_5 (Aldrich, 99.99%) served as the starting materials for the solid-state reaction method and were utilized without any additional purification. Double-doped lithium garnets, denoted as LALZN, were synthesized with a target composition of $\text{Li}_{7-3x}\text{Al}_x\text{La}_3\text{Zr}_{2-(5/4)y}\text{Nb}_y\text{O}_{12}$ (LALZN). The doping concentrations for Al and Nb were systematically varied, with combinations of (x, y) as follows: (0.20, 0.20), (0.20, 0.25), (0.25, 0.20), (0.25, 0.25), and (0.3, 0.3). An additional 15 wt% of Li_2CO_3 was incorporated to mitigate lithium loss during high-temperature sintering.

The precursor materials were subjected to ball milling using a Pulverisette 7, Fritsch with zirconia balls in isopropanol for a duration of 12 h at a speed of 250 rpm. Following the ball milling, the powders were heated at 80 °C for 24 h to evaporate residual solvents. Subsequently, the powders were manually ground using a mortar and pestle and then annealed at 900 °C for 12 h. The resulting powders were further ground and ball-milled for an additional 12 h. After ensuring complete solvent evaporation,

the powders were pelletized under a pressure of 65 MPa. Prior to the final sintering at 1130 °C for 12 h, the pellets were coated with powder of the same composition to prevent lithium loss during the sintering process.

2.2. Analysis of materials and electrochemical properties

After sintering, one of the pellets was subjected to grinding and characterized via X-ray diffraction (XRD) using a D/MAX Ultima III, Rigaku diffractometer equipped with Cu K α radiation. The surface morphology of the pellets was examined using field-emission scanning electron microscopy (FE-SEM; Hitachi S-4700).

For conductivity measurements, pellet surfaces were polished using abrasive papers with grit sizes of 180, 400, and 2000, corresponding to diameters of 82–12.6 mm. To ensure optimal interface interactions, ceramic pellets of 18 mm diameter and 0.3 mm thickness were sputtered with a platinum film on both surfaces. Subsequently, silver paste was applied and the samples were annealed at 500 °C for 2 h. The lithium-ion conductivity of LLZO ceramics was determined by analyzing impedance spectra captured using a ZIVE SP2 impedance analyzer over a frequency range of 1 Hz to 1 MHz. A voltage amplitude of 100 mV was maintained at open circuit potential. For AC-impedance experiments, the pellets were first sputtered with platinum and then coated with silver paste on both sides after undergoing sintering at 1130 °C for 12 h. Silver, serving as a non-blocking electrode, was subsequently sintered at 500 °C to enhance contact with the LLZO pellets.

Pellet conductivity was deduced using the formula $\sigma = 1/R \times (T/A)$, where 'R' denotes the pellet resistance measurable by the impedance on the real axis of the Nyquist plot, 'T' is the thickness of the ceramic disc, and 'A' represents the surface area. Impedance measurements were taken across a temperature range of 25 to 50°C. The activation energy was assessed from the temperature-dependent ionic conductivity of the pellets, employing the Arrhenius equation.

3. Results and Discussion

3.1. Effects of double doping with Al and Nb on the crystal structure and microstructure of LALZN

To understand potential synergistic effects, both Al and

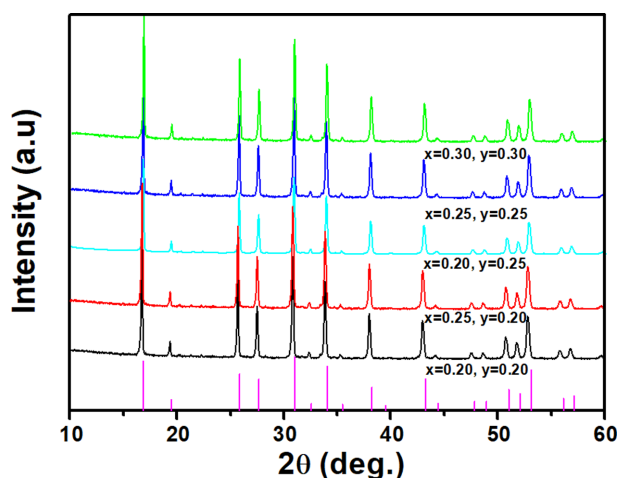


Fig. 1. XRD patterns of LALZNO garnets with varying concentrations of simultaneous Al and Nb doping, post-sintering at 1130 °C for 12 h

Nb were doped simultaneously at various concentrations, aiming to optimize their combined effect on ionic conductivity. Fig. 1 presents the XRD patterns of $\text{Li}_{7-3x}\text{Al}_x\text{La}_3\text{Zr}_{2-(5/4)y}\text{Nb}_y\text{O}_{12}$ for the combinations: $x = 0.20, y = 0.20$; $x = 0.25, y = 0.20$; $x = 0.20, y = 0.25$; $x = 0.25, y = 0.25$; and $x = 0.30, y = 0.30$. All peaks exhibited sharpness and closely aligned with the cubic phase reference (JCPDS 45-0109), irrespective of the variations in Al and Nb concentrations. No additional peaks or impurity phases were observed for any composition of the double-doped LALZN. The XRD analysis suggests that doping with 0.20 mol each of Al and Nb in LLZO results in a pure cubic phase. Increasing concentrations of Al or Nb did not introduce any extraneous or impure phases, maintaining the cubic structure. These patterns for the dual-doped LLZO align with previously reported results [4].

The SEM images of the double-doped LLZO are presented in Fig. 2. These images consistently reveal a non-porous, dense morphology with pronounced particle agglomeration across all examined concentrations of Al and Nb in the LLZO samples. Notably, variations between different doping levels are subtle. The LLZO doped with 0.20 mol each of Al and Nb exhibits a more interconnected and distinctly crystallized surface. By increasing the Al concentration to 0.25 mol, while keeping the Nb concentration constant, the morphology becomes more interconnected. This observation aligns with prior discussions regarding the influence of Al on LLZO.

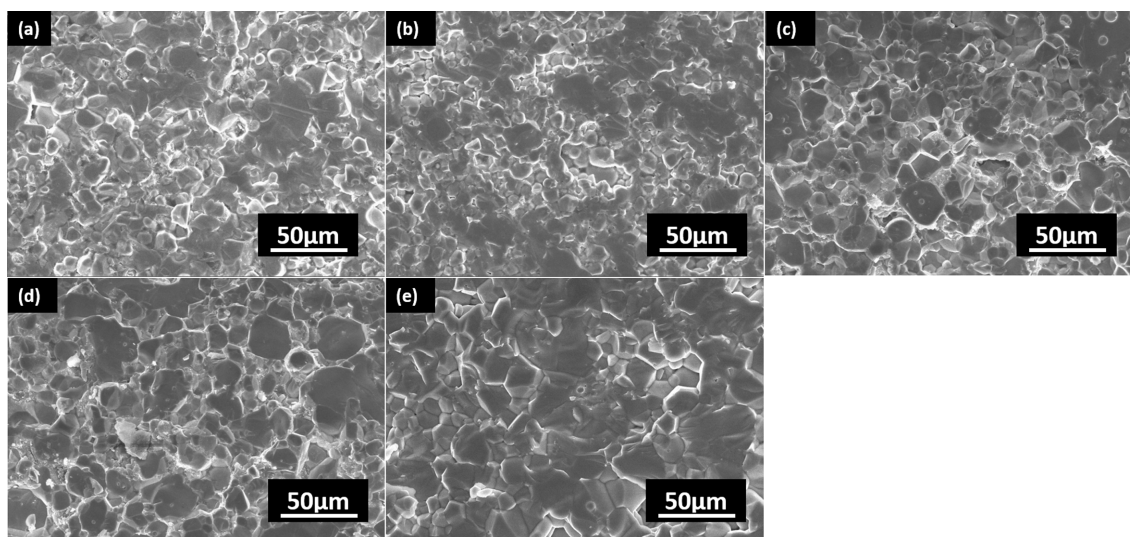


Fig. 2. SEM images of $\text{Li}_{7-3x}\text{Al}_x\text{La}_3\text{Zr}_{2-(5/4)y}\text{Nb}_y\text{O}_{12}$ for the following concentrations: (a) $x = 0.20$, $y = 0.20$; (b) $x = 0.25$, $y = 0.20$; (c) $x = 0.20$, $y = 0.25$; (d) $x = 0.25$, $y = 0.25$; and (e) $x = 0.30$, $y = 0.30$

Conversely, increasing the Nb concentration to 0.25 mol, while maintaining a constant Al concentration, results in a slightly improved morphology. This is attributed to Nb's tendency to enlarge grain size and enhance surface densification. Our analysis suggests that in this dual-doping scenario, Nb exerts a slightly more pronounced effect than Al. The optimal morphology—characterized by robust particle agglomeration and a dense surface, which is conducive to efficient Li-ion conduction—was observed in the LLZO sample with 0.30 mol doping of both Al and Nb. This enhanced morphology, resulting from increased doping levels of both elements, showcases the combined benefits of Al and Nb. The morphological findings presented herein align with those reported in other studies [41].

3.2. Influence of combined Al and Nb doping on the conductivity of LALZN

Fig. 3a presents Nyquist plots at 30 °C for LLZO with various simultaneous doping levels of Al in Li and Nb in Zr. The appearance of a single semicircle, rather than two, suggests that distinct contributions from grains and grain boundaries may overlap, potentially leading to indistinguishable regions [43]. Nevertheless, it can be inferred that the high-frequency interception pertains to the bulk, where no semicircle manifests, and the low-frequency interception is associated with grain boundary contributions. The suppressed shapes of the four

impedance spectra align with previously reported dense, conductive LLZO structures [44]. Fig. 3b, c, and d respectively depict the bulk, grain boundary, and total conductivity as functions of the Al and Nb doping levels in LLZO. The minimum observed bulk and grain boundary conductivities were 6.32×10^{-4} and 1.38×10^{-4} S cm^{-1} , respectively, for the LLZO doped with 0.20 mol each of Al and Nb (Fig. 3c). This yielded a total ionic conductivity of 1.15×10^{-4} S cm^{-1} for this composition, which is superior to the values for LLZO doped only with Al or Nb (Fig. 3d). This enhancement can be attributed to the synergistic effects of dual doping: Al doping in Li sites creates vacancies, leading to a stable cubic phase with Li disorder over octahedral sites, while Nb doping in Zr facilitates Li ion charge carrier fine-tuning, augmenting carrier mobility and balancing Li ion concentration [42]. As the doping levels of Al and Nb varied, a range of conductivity values was observed, with slight differences among them. The peak total ionic conductivity, 1.44×10^{-4} S cm^{-1} , was achieved with 0.30 mol doping of both Al and Nb.

The temperature-dependent ionic conductivity of dual-doped LLZO, incorporating various concentrations of Al and Nb and sintered at 1130 °C for 12h, is illustrated in Fig. 4a according to the Arrhenius equation. The associated activation energies for these compositions are presented in Fig. 4b. The peak activation energy, recorded at 0.48 eV, corresponded to the lowest total ionic

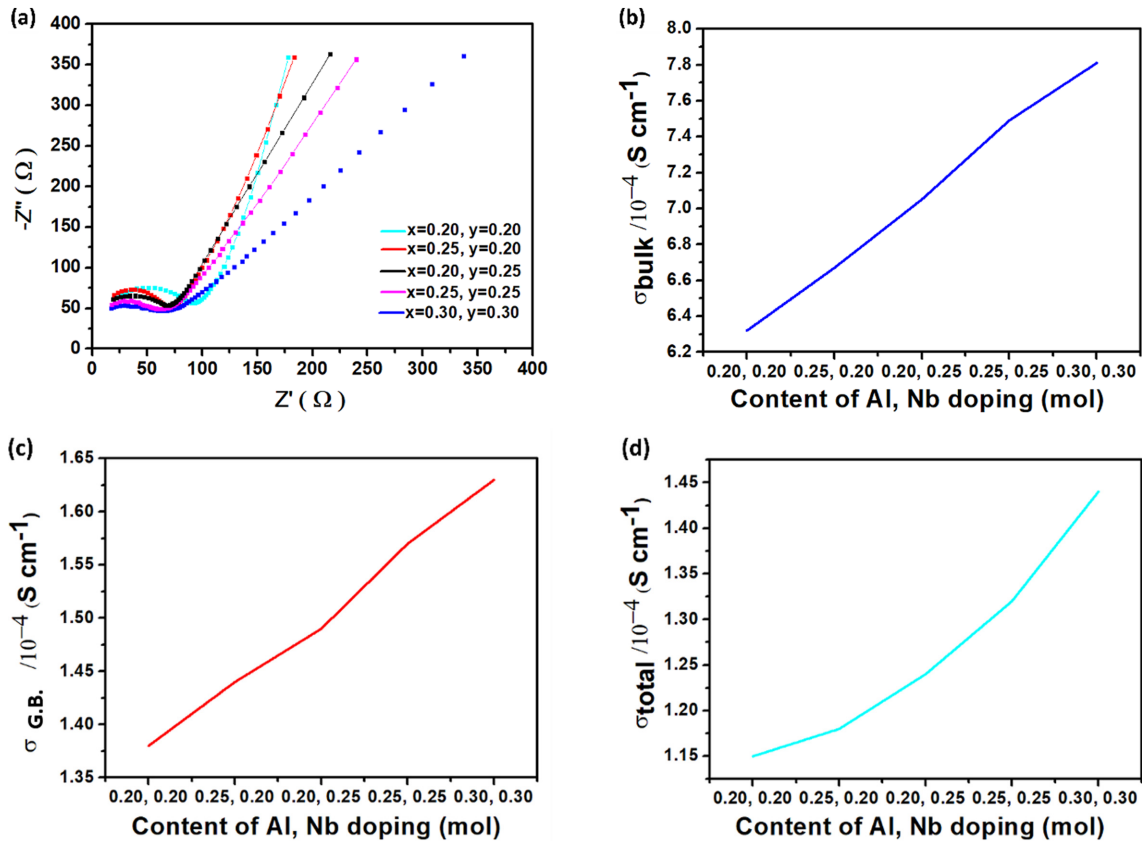


Fig. 3. (a) Nyquist plots of LALZN samples at 30 °C with varying concentrations of Nb doping; (b) bulk conductivities; (c) grain boundary conductivities; and (d) total conductivities as functions of Al and Nb dopant content, respectively

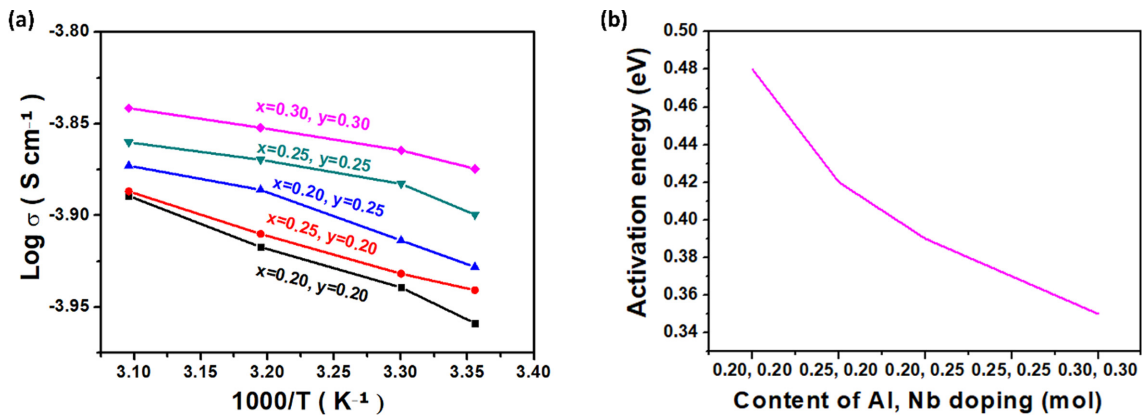


Fig. 4. (a) Arrhenius plots of the double-doped LALZN conductivity for various concentrations of Al and Nb doping; and (b) calculated activation energies for the LALZN electrolytes based on various concentrations of Al and Nb doping

conductivity observed for the 0.20 mol of both Al and Nb dopants in LLZO. Upon increasing Al to 0.25 mol, the activation energy reduced to 0.42 eV, resulting in a marginal increase in total ionic conductivity. Similarly, an augmentation of the Nb dopant to 0.25 mol led to a further reduction in activation energy to 0.39 eV, paralleled by an increase in conductivity. The highest total ionic

conductivity was observed for a dopant content of 0.25 mol for both Al and Nb, with the activation energy being the lowest at 0.37 eV, underscoring the role of reduced activation energy in enhancing ionic conductivity. This trend—decreasing activation energy and increasing ionic conductivity with rising dopant concentration—aligns with previously reported findings [10,33]. In these Al-Nb

Table 1. Bulk, grain boundary, and total ionic conductivities, activation energies, and area-specific resistances for various concentrations of LALZN samples

Doping amount x, y	Bulk conductivity σ_{bulk} [S cm ⁻¹]	Grain boundary conductivity σ_{grain} [S cm ⁻¹]	Total ionic conductivity σ_{total} [S cm ⁻¹]	Activation energy E_a [eV]	Area specific resistance [Ω cm ²]
0.20, 0.20	6.32×10^{-4}	1.38×10^{-4}	1.15×10^{-4}	0.48	106
0.25, 0.20	6.67×10^{-4}	1.44×10^{-4}	1.18×10^{-4}	0.42	103
0.20, 0.25	7.05×10^{-4}	1.49×10^{-4}	1.24×10^{-4}	0.39	99
0.25, 0.25	7.49×10^{-4}	1.57×10^{-4}	1.32×10^{-4}	0.37	94
0.30, 0.30	7.81×10^{-4}	1.63×10^{-4}	1.44×10^{-4}	0.37	90

dual-doped LLZO samples with elevated concentrations, the Li diffusion pathway was expanded by Al [45], aiding Li-ion diffusivity. Additionally, a higher Al concentration promoted grain connectivity, while Nb facilitated LLZO densification. Collectively, these factors markedly improved the ionic conductivity of LLZO [41]. Comprehensive data on bulk, grain boundary, total ionic

conductivities, activation energies, and area-specific resistances are provided in Table 1.

3.3. Influence of combined Al and Nb doping on the electrochemical performance of LALZN

Fig. 5a presents the Nyquist plots for the cell with a composition of $\text{Li}_{7-3x}\text{Al}_x\text{La}_3\text{Zr}_{2-(5/4)y}\text{Nb}_y\text{O}_{12}$ where $x = y =$

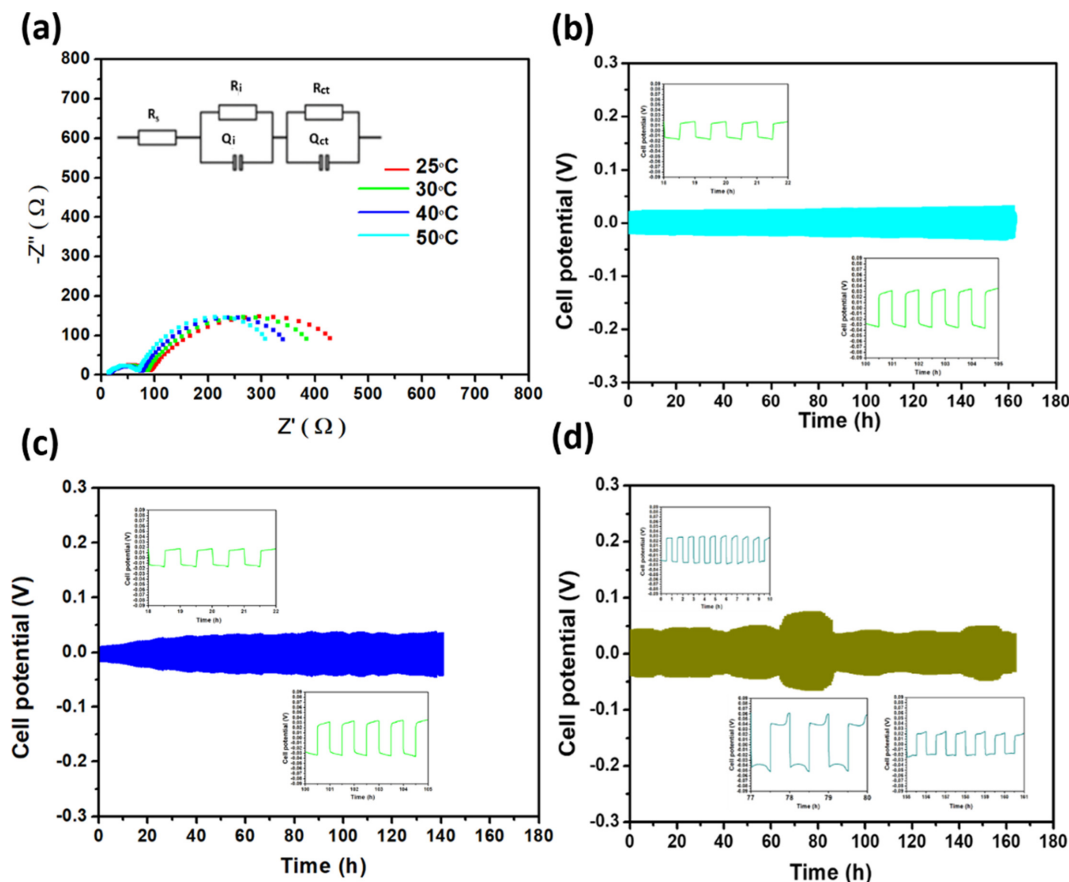


Fig. 5. (a) EIS profiles of the symmetric cell of $\text{Li}/\text{SP}/\text{LALZN}/\text{SP}/\text{Li}$, where $x = y = 0.25$, at various temperatures. Cell potential profile for the symmetric cell ($\text{Li}/\text{SP}/\text{LALZN}/\text{SP}/\text{Li}$): (b) where $\text{Al} = \text{Nb} = 0.25$ mol, under 0.1 mA cm^{-2} at $30 \text{ }^\circ\text{C}$; (c) where $\text{Al} = \text{Nb} = 0.20$ mol, under 0.1 mA cm^{-2} ; (d) where $\text{Al} = \text{Nb} = 0.25$ mol, under 0.2 mA cm^{-2}

0.25. The left semicircle in this impedance spectrum is attributed to the total resistance of the garnet material, consistent with the resistance observed for the synthesized LALZN. The total resistance of the solid electrolyte, derived from this EIS plot, was approximately 92 W cm^2 . The charge transfer resistance was found to be around 450 W cm^2 at $30 \text{ }^\circ\text{C}$. This is higher than that of the symmetric cell composed of singly doped Al and Nb LLZO. The LLZO synthesized with dual doping of 0.30 mol Al and Nb exhibited a denser morphology and superior ionic conductivity compared to both singly doped and other dual-doped LLZO variants.

To assess the electrochemical performance of the dual-doped LLZO, a galvanostatic charge-discharge analysis was conducted using a symmetric cell composed of $\text{Li}_{7-3x}\text{Al}_x\text{La}_3\text{Zr}_{2-(5/4)y}\text{Nb}_y\text{O}_{12}$, where $x = y = 0.25$. This was performed at a current density of 0.1 mA cm^{-2} with 30 min intervals between each charge-discharge step. The voltage profile in Fig. 5b exhibited minimal polarization, remaining

below 0.03 V for the first 100 h. Beyond 100 h, a slight increase in polarization to approximately 0.03 V was noted. The stability of the voltage profile even after 170 h underscores the outstanding cycling performance offered by this dual-doped LLZO.

For comparative analysis, a symmetric cell with a solid electrolyte composition of $\text{Li}_{7-3x}\text{Al}_x\text{La}_3\text{Zr}_{2-(5/4)y}\text{Nb}_y\text{O}_{12}$, where $x = y = 0.20$, was evaluated as shown in Fig.5c. While the cell showcased a low overpotential of 0.01 V during the initial 10 h of cycling, which was less than that observed for the 0.25 mol dual-doped LALZN, a noticeable increase in polarization to 0.04 V was seen after 15 h. This level of polarization, although higher than that of the 0.25 mol dual-doped LLZO, remains acceptable for symmetric cell operations. The higher polarization in the 0.20 mol doped LALZN can be attributed to its marginally lower ionic conductivity compared to the 0.25 mol variant. Consequently, variations in the ionic conductivities of these solid electrolytes are the primary factors responsible

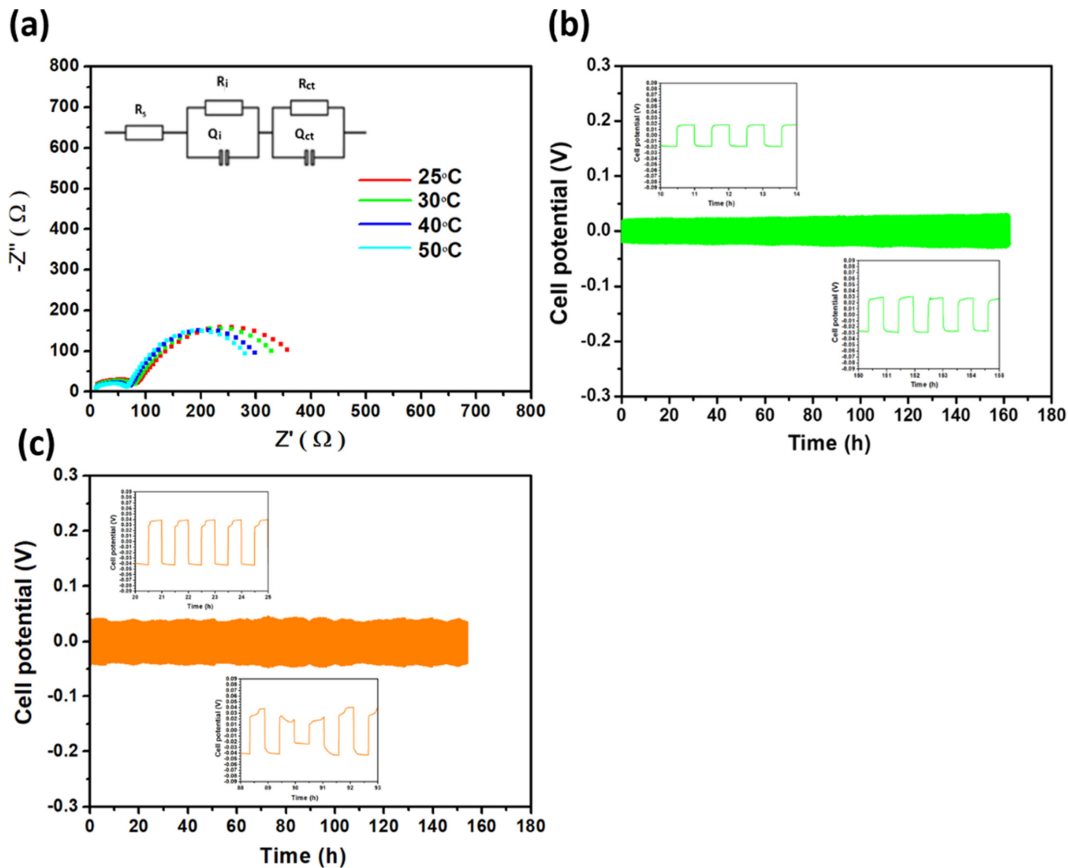


Fig. 6. (a) EIS profiles of the symmetric cell of Li/SP/LALZN/SP/Li, where $x = y = 0.30$, at various temperature. Cell potential profile for the symmetric cell (Li/SP/LALZN/SP/Li); (b) where $\text{Al} = \text{Nb} = 0.30 \text{ mol}$, under 0.1 mA cm^{-2} at $30 \text{ }^\circ\text{C}$; where $\text{Al} = \text{Nb} = 0.30 \text{ mol}$, under 0.2 mA cm^{-2}

for differences in ohmic polarization.

The cell, featuring the solid garnet $\text{Li}_{7-3x}\text{Al}_x\text{La}_3\text{Zr}_{2-(5/4)y}\text{Nb}_y\text{O}_{12}$ composition where $x = y = 0.25$, was subjected to cycling at 0.2 mA cm^{-2} for 170 h, as depicted in Fig. 5d. The time-dependent cycling performance shown in Fig. 5d indicates that the symmetric cell maintained a minimal overpotential of approximately 0.03 V at a high current density of 0.2 mA cm^{-2} , albeit with some variations. In comparison, the potential profile of the symmetric cell with 0.20 mol dual-doped LALZN exhibited a slightly elevated potential of 0.04 V relative to the 0.25 mol doped LALZN, a discrepancy attributable to the differences in ionic conductivity. Both symmetric cells demonstrated an unstable voltage profile characterized by minimal ohmic polarization at 0.2 mA cm^{-2} . This suggests that as the current increases, voltage fluctuations and a slight rise in polarization can be observed. Nevertheless, the garnet material is undeniably valuable for integration into solid-liquid Li-ion cells, given its low overpotential.

The Nyquist plots for the symmetric cell configuration Li/SP/LALZN/SP/Li, where $x = y = 0.30$, are presented in Fig. 6a. Given that the solid electrolyte with 0.30 mol dual-doping of Al and Nb previously displayed the highest ionic conductivity, the total resistance of this symmetric cell was observed to be lower than that of the 0.30 mol dual-doped sample. The measured total resistance was approximately 400 W cm^2 , leading to reduced charge transfer and interfacial resistances.

Fig. 6b illustrates the cell potential profile at a current density of 0.1 mA cm^{-2} . The observed overpotential was minimal, less than 0.02 V, and displayed a stable charge-discharge plateau. Given that the solid electrolyte with 0.30 mol dual doping exhibited the highest ionic conductivity, the symmetric cell employing this electrolyte demonstrated the lowest overpotential. With an increase in current density, a slight rise in cell potential was observed. At a current density of 0.2 mA cm^{-2} , the symmetric cell exhibited an overpotential of 0.04 V, slightly higher than the earlier value presented in Fig. 6c. In all tests, symmetric cells at current densities of 0.1 and 0.2 mA cm^{-2} , using solid electrolytes with various dopant amounts, consistently displayed minimal overpotentials in their charge-discharge profiles. Consequently, it is evident that our solid electrolyte holds promise as a viable candidate for Li-ion batteries.

4. Conclusions

Fine Al and Nb doped- $\text{Li}_{7-x}\text{Al}_x\text{La}_3\text{Zr}_{2-(5/4)y}\text{Nb}_y\text{O}_{12}$ (LALZN) powders were synthesized at $900 \text{ }^\circ\text{C}$ using the solid-state reaction method. The dual-doped LALZN demonstrated a pure cubic phase at a 0.20 mol Al and Nb co-doping level. The peak ionic conductivity achieved was $1.44 \times 10^{-4} \text{ S cm}^{-1}$ for the 0.30 mol dual-doped LALZN. The symmetric cells composed of Li/Separator/LALZN/Separator/Li showcased commendable cycling performances at both 0.1 and 0.2 mA cm^{-2} current densities, demonstrating extended cycle life. In particular, the dual-doped LLZO materials show promise for incorporation into full cells. With further optimization, particularly concerning molten Li metal interactions and the interfacial dynamics between Li and LLZO, our synthesized garnet solid electrolyte holds potential for utilization in all-solid-state Li-ion batteries.

Acknowledgements

This work was supported by the National Research Foundation of Korea (NRF) grant funded by the MSIT, Korea (No. 2019R1A2C1084020 and No. 2018R1A5A1025224).

References

1. M. Kotobuki and M. Koishi, Preparation of $\text{Li}_7\text{La}_3\text{Zr}_2\text{O}_{12}$ solid electrolyte via a sol-gel method, *Ceramics International*, **40**, 5043 (2014). Doi: <https://doi.org/10.1016/j.ceramint.2013.09.009>
2. Y. Mizuno, H. Wagata, H. Onodera, K. Yubuta, T. Shishido, S. Oishi, and K. Teshima, Environmentally Friendly Flux Growth of High-Quality, Idiomorphic $\text{Li}_3\text{La}_3\text{Nb}_2\text{O}_{12}$ Crystals, *Crystal Growth & Design*, **13**, 479 (2013). Doi: <https://doi.org/10.1021/cg3012348>
3. A. Ramzy and V. Thangadurai, Tailor-Made Development of Fast Li Ion Conducting Garnet-Like Solid Electrolytes, *ACS Applied Materials & Interfaces*, **2**, 385 (2010). Doi: <https://doi.org/10.1021/am900643t>
4. L. Dhivya and R. Murugan, Effect of Simultaneous Substitution of Y and Ta on the Stabilization of Cubic Phase, Microstructure, and Li^+ Conductivity of $\text{Li}_7\text{La}_3\text{Zr}_2\text{O}_{12}$ Lithium Garnet, *S Applied Materials & Interfaces*, **6**, 17606 (2014). Doi: <https://doi.org/10.1021/am503731h>
5. W. G. Zeier, S. Zhou, B. Lopez-Bermudez, K. Page, and

- B. C. Melot, Dependence of the Li-Ion Conductivity and Activation Energies on the Crystal Structure and Ionic Radii in $\text{Li}_6\text{MLa}_2\text{Ta}_2\text{O}_{12}$, *ACS Applied Materials & Interfaces*, **6**, 10900 (2014). Doi: <https://doi.org/10.1021/am4060194>
6. H. Zhang, C. Li, M. Piszcz, E. Coya, T. Rojo, L.M. Rodriguez-Martinez, M. Armand, and Z. Zhou, Single lithium-ion conducting solid polymer electrolytes: advances and perspectives, *Chemical Society Reviews*, **46**, 797 (2017). Doi: <https://doi.org/10.1039/C6CS00491A>
 7. C. K. Chan, T. Yang, and J. Mark Weller, Nanostructured Garnet-type $\text{Li}_7\text{La}_3\text{Zr}_2\text{O}_{12}$: Synthesis, Properties, and Opportunities as Electrolytes for Li-ion Batteries, *Electrochimica Acta*, **253**, 268 (2017). Doi: <https://doi.org/10.1016/j.electacta.2017.08.130>
 8. J. H. Kim, Interfacial Reaction between Li Metal and Solid Electrolyte in All-Solid-State Batteries, *Corrosion Science and Technology*, **22**, 287 (2023). Doi: <https://doi.org/10.14773/CST.2023.22.4.287>
 9. J. Zhang, N. Zhao, M. Zhang, Y. Li, P.K. Chu, X. Guo, Z. Di, X. Wang, and H. Li, Flexible and ion-conducting membrane electrolytes for solid-state lithium batteries: Dispersion of garnet nanoparticles in insulating polyethylene oxide, *Nano Energy*, **28**, 447 (2016). Doi: <https://doi.org/10.1016/j.nanoen.2016.09.002>
 10. J. -F. Wu, W. K. Pang, V. K. Peterson, L. Wei, and X. Guo, Garnet-Type Fast Li-Ion Conductors with High Ionic Conductivities for All-Solid-State Batteries, *ACS Applied Materials & Interfaces*, **9**, 12461 (2017). Doi: <https://doi.org/10.1021/acsami.7b00614>
 11. K. Aso, A. Sakuda, A. Hayashi, and M. Tatsumisago, All-Solid-State Lithium Secondary Batteries Using NiS-Carbon Fiber Composite Electrodes Coated with $\text{Li}_2\text{S-P}_2\text{S}_5$ Solid Electrolytes by Pulsed Laser Deposition, *ACS Applied Materials & Interfaces*, **5**, 686 (2013). Doi: <https://doi.org/10.1021/am302164e>
 12. Y. Kato, S. Hori, T. Saito, K. Suzuki, M. Hirayama, A. Mitsui, M. Yonemura, H. Iba, and R. Kanno, High-power all-solid-state batteries using sulfide superionic conductors, *Nature Energy*, **1**, 16030 (2016). Doi: <https://doi.org/10.1038/nenergy.2016.30>
 13. Y. Seino, T. Ota, K. Takada, A. Hayashi, M. Tatsumisago, A sulphide lithium super ion conductor is superior to liquid ion conductors for use in rechargeable batteries, *Energy & Environmental Science*, **7**, 627 (2014). Doi: <https://doi.org/10.1039/C3EE41655K>
 14. L. J. Miara, N. Suzuki, W. D. Richards, Y. Wang, J. C. Kim, and G. Ceder, Li-ion conductivity in $\text{Li}_9\text{S}_3\text{N}$, *Journal of Materials Chemistry A*, **3**, 20338 (2015). Doi: <https://doi.org/10.1039/C5TA05432J>
 15. K. Arbi, J.M. Rojo, and J. Sanz, Lithium mobility in titanium based Nasicon $\text{Li}_{1+x}\text{Ti}_{2-x}\text{Al}_x(\text{PO}_4)_3$ and $\text{LiTi}_{2-x}\text{Zr}_x(\text{PO}_4)_3$ materials followed by NMR and impedance spectroscopy, *Journal of the European Ceramic Society*, **27**, 4215 (2007). Doi: <https://doi.org/10.1016/j.jeurceramsoc.2007.02.118>
 16. N. Kamaya, K. Homma, Y. Yamakawa, M. Hirayama, R. Kanno, M. Yonemura, T. Kamiyama, Y. Kato, S. Hama, K. Kawamoto, and A. Mitsui, A lithium superionic conductor, *Nature Materials*, **10**, 682 (2011). Doi: <https://doi.org/10.1038/nmat3066>
 17. R. Murugan, V. Thangadurai, and W. Weppner, Fast Lithium Ion Conduction in Garnet-Type $\text{Li}_7\text{La}_3\text{Zr}_2\text{O}_{12}$, *Angewandte Chemie International Edition*, **46**, 7778 (2007). Doi: <https://doi.org/10.1002/anie.200701144>
 18. S. Xuefu, H. Nemori, S. Mitsuoka, P. Xu, M. Matsui, Y. Takeda, O. Yamamoto, and N. Imanishi, High Lithium-Ion-Conducting NASICON-Type $\text{Li}_{1+x}\text{Al}_x\text{Ge}_y\text{Ti}_{2-x-y}(\text{PO}_4)_3$ Solid Electrolyte, *Frontiers in Energy Research*, **4**, 12 (2016). Doi: <https://doi.org/10.3389/fenrg.2016.00012>
 19. F. Han, T. Gao, Y. Zhu, K.J. Gaskell, and C. Wang, A Battery Made from a Single Material, *Advanced Materials*, **27**, 3473 (2015). Doi: <https://doi.org/10.1002/adma.201500180>
 20. M. Kotobuki, H. Munakata, K. Kanamura, Y. Sato, and T. Yoshida, Compatibility of $\text{Li}_7\text{La}_3\text{Zr}_2\text{O}_{12}$ Solid Electrolyte to All-Solid-State Battery Using Li Metal Anode, *Journal of The Electrochemical Society*, **157**, A1076 (2010). Doi: <https://doi.org/10.1149/1.3474232>
 21. K. Kajihara, N. Tezuka, M. Shoji, J. Wakasugi, H. Munakata, and K. Kanamura, $\text{Li}_4\text{B}_4\text{M}_3\text{O}_{12}\text{Cl}$ ($M = \text{Al}, \text{Ga}$): An Electrochemically Stable, Lithium-Ion-Conducting Cubic Boracite with Substituted Boron Sites, *Bulletin of the Chemical Society of Japan*, **90**, 1279 (2017). Doi: <https://doi.org/10.1246/bcsj.20170242>
 22. J. Awaka, N. Kijima, H. Hayakawa, and J. Akimoto, Synthesis and structure analysis of tetragonal $\text{Li}_7\text{La}_3\text{Zr}_2\text{O}_{12}$ with the garnet-related type structure, *Journal of Solid State Chemistry*, **182**, 2046 (2009). Doi: <https://doi.org/10.1016/j.jssc.2009.05.020>
 23. R. Wagner, G. J. Redhammer, D. Rettenwander, A. Senyshyn, W. Schmidt, M. Wilkening, and G. Amthauer, Crystal Structure of Garnet-Related Li-Ion Conductor $\text{Li}_{7-3x}\text{Ga}_x\text{La}_3\text{Zr}_2\text{O}_{12}$: Fast Li-Ion Conduction Caused by a Different Cubic Modification?, *Chemistry of Materials*,

- 28**, 1861 (2016). Doi: <https://doi.org/10.1021/acs.chemmater.6b00038>
24. C. A. Geiger, E. Alekseev, B. Lazic, M. Fisch, T. Armbruster, R. Langner, M. Fechtelkord, N. Kim, T. Pettke, and W. Weppner, Crystal Chemistry and Stability of “ $\text{Li}_7\text{La}_3\text{Zr}_2\text{O}_{12}$ ” Garnet: A Fast Lithium-Ion Conductor, *Inorganic Chemistry*, **50**, 1089 (2011). Doi: <https://doi.org/10.1021/ic101914e>
 25. N. Bernstein, M. D. Johannes, and K. Hoang, Origin of the Structural Phase Transition in $\text{Li}_7\text{La}_3\text{Zr}_2\text{O}_{12}$, *Physical Review Letters*, **109**, 205702 (2012). Doi: <https://doi.org/10.1103/PhysRevLett.109.205702>
 26. A. Düvel, A. Kuhn, L. Robben, M. Wilkening, and P. Heitjans, Mechano-synthesis of Solid Electrolytes: Preparation, Characterization, and Li Ion Transport Properties of Garnet-Type Al-Doped $\text{Li}_7\text{La}_3\text{Zr}_2\text{O}_{12}$ Crystallizing with Cubic Symmetry, *The Journal of Physical Chemistry C*, **116**, 15192 (2012). Doi: <https://doi.org/10.1021/jp301193r>
 27. S. Afyon, F. Krumeich, and J. L. M. Rupp, A shortcut to garnet-type fast Li-ion conductors for all-solid state batteries, *Journal of Materials Chemistry A*, **3**, 18636 (2015). Doi: <https://doi.org/10.1039/C5TA03239C>
 28. R. Jalem, M. J. D. Rushton, W. Manalastas, M. Nakayama, T. Kasuga, J. A. Kilner, and R. W. Grimes, Effects of Gallium Doping in Garnet-Type $\text{Li}_7\text{La}_3\text{Zr}_2\text{O}_{12}$ Solid Electrolytes, *Chemistry of Materials*, **27**, 2821 (2015). Doi: <https://doi.org/10.1021/cm5045122>
 29. F. Aguesse, W. Manalastas, L. Buannic, J.M. Lopez del Amo, G. Singh, A. Llordés, and J. Kilner, Investigating the Dendritic Growth during Full Cell Cycling of Garnet Electrolyte in Direct Contact with Li Metal, *ACS Applied Materials & Interfaces*, **9**, 3808 (2017). Doi: <https://doi.org/10.1021/acsami.6b13925>
 30. D. Rettenwander, C. A. Geiger, M. Tribus, P. Tropper, and G. Amthauer, A Synthesis and Crystal Chemical Study of the Fast Ion Conductor $\text{Li}_{7-3x}\text{Ga}_x\text{La}_3\text{Zr}_2\text{O}_{12}$ with $x = 0.08$ to 0.84 , *Inorganic Chemistry*, **53**, 6264 (2014). Doi: <https://doi.org/10.1021/ic500803h>
 31. J. -F. Wu, E. -Y. Chen, Y. Yu, L. Liu, Y. Wu, W. K. Pang, V. K. Peterson, and X. Guo, Gallium-Doped $\text{Li}_7\text{La}_3\text{Zr}_2\text{O}_{12}$ Garnet-Type Electrolytes with High Lithium-Ion Conductivity, *ACS Applied Materials & Interfaces*, **9**, 1542 (2017). Doi: <https://doi.org/10.1021/acsami.6b13902>
 32. A. K. Baral, S. Narayanan, F. Ramezanipour, and V. Thangadurai, Evaluation of fundamental transport properties of Li-excess garnet-type $\text{Li}_{5+2x}\text{La}_3\text{Ta}_{2-x}\text{Y}_x\text{O}_{12}$ ($x = 0.25, 0.5$ and 0.75) electrolytes using AC impedance and dielectric spectroscopy, *Physical Chemistry Chemical Physics*, **16**, 11356 (2014). Doi: <https://doi.org/10.1039/C4CP00418C>
 33. S. Ramakumar, L. Satyanarayana, S. V. Manorama, and R. Murugan, Structure and Li^+ dynamics of Sb-doped $\text{Li}_7\text{La}_3\text{Zr}_2\text{O}_{12}$ fast lithium ion conductors, *Physical Chemistry Chemical Physics*, **15**, 11327 (2013). Doi: <https://doi.org/10.1039/C3CP50991E>
 34. Y. Li, Z. Wang, Y. Cao, F. Du, C. Chen, Z. Cui, and X. Guo, W-Doped $\text{Li}_7\text{La}_3\text{Zr}_2\text{O}_{12}$ Ceramic Electrolytes for Solid State Li-ion Batteries, *Electrochimica Acta*, **180**, 37 (2015). Doi: <https://doi.org/10.1016/j.electacta.2015.08.046>
 35. Y. Li, J.-T. Han, C.-A. Wang, H. Xie, and J.B. Goodenough, Optimizing Li^+ conductivity in a garnet framework, *Journal of Materials Chemistry*, **22**, 15357 (2012). Doi: <https://doi.org/10.1039/C2JM31413D>
 36. S. Ohta, T. Kobayashi, and T. Asaoka, High lithium ionic conductivity in the garnet-type oxide $\text{Li}_{7-x}\text{La}_3(\text{Zr}_{2-x}\text{Nb}_x)\text{O}_{12}$ ($X = 0-2$), *Journal of Power Sources*, **196**, 3342 (2011). Doi: <https://doi.org/10.1016/j.jpowsour.2010.11.089>
 37. A. Dumon, M. Huang, Y. Shen, and C. W. Nan, High Li ion conductivity in strontium doped $\text{Li}_7\text{La}_3\text{Zr}_2\text{O}_{12}$ garnet, *Solid State Ionics*, **243**, 36 (2013). Doi: <https://doi.org/10.1016/j.ssi.2013.04.016>
 38. E. Rangasamy, J. Wolfenstine, J. Allen, and J. Sakamoto, The effect of 24c-site (A) cation substitution on the tetragonal–cubic phase transition in $\text{Li}_{7-x}\text{La}_{3-x}\text{A}_x\text{Zr}_2\text{O}_{12}$ garnet-based ceramic electrolyte, *Journal of Power Sources*, **230**, 261 (2013). Doi: <https://doi.org/10.1016/j.jpowsour.2012.12.076>
 39. Y. Kihira, S. Ohta, H. Imagawa, and T. Asaoka, Effect of Simultaneous Substitution of Alkali Earth Metals and Nb in $\text{Li}_7\text{La}_3\text{Zr}_2\text{O}_{12}$ on Lithium-Ion Conductivity, *ECS Electrochemistry Letters*, **2**, A56 (2013). Doi: <https://doi.org/10.1149/2.001307eel>
 40. D. O. Shin, K. Oh, K. M. Kim, K. -Y. Park, B. Lee, Y. -G. Lee, and K. Kang, Synergistic multi-doping effects on the $\text{Li}_7\text{La}_3\text{Zr}_2\text{O}_{12}$ solid electrolyte for fast lithium ion conduction, *Scientific Reports*, **5**, 18053 (2015). Doi: <https://doi.org/10.1038/srep18053>
 41. T. Yang, Y. Li, W. Wu, Z. Cao, W. He, Y. Gao, J. Liu, and G. Li, The synergistic effect of dual substitution of Al and Sb on structure and ionic conductivity of $\text{Li}_7\text{La}_3\text{Zr}_2\text{O}_{12}$ ceramic, *Ceramics International*, **44**, 1538 (2018). Doi: <https://doi.org/10.1016/j.ceramint.2017.10.072>
 42. L. Buannic, B. Orayech, J.-M. López Del Amo, J. Car-

- rasco, N. A. Katcho, F. Aguesse, W. Manalastas, W. Zhang, J. Kilner, and A. Llordés, Dual Substitution Strategy to Enhance Li⁺ Ionic Conductivity in Li₇La₃Zr₂O₁₂ Solid Electrolyte, *Chemistry of Materials*, **29**, 1769 (2017). Doi: <https://doi.org/10.1021/acs.chemmater.6b05369>
43. C. Deviannapoorani, L. Dhivya, S. Ramakumar, and R. Murugan, Lithium ion transport properties of high conductive tellurium substituted Li₇La₃Zr₂O₁₂ cubic lithium garnets, *Journal of Power Sources*, **240**, 18 (2013). Doi: <https://doi.org/10.1016/j.jpowsour.2013.03.166>
44. K. Fu, Y. Gong, B. Liu, Y. Zhu, S. Xu, Y. Yao, W. Luo, C. Wang, S. D. Lacey, J. Dai, Y. Chen, Y. Mo, E. Wachsmann, and L. Hu, Toward garnet electrolyte-based Li metal batteries: An ultrathin, highly effective, artificial solid-state electrolyte/metallic Li interface, *Science Advances*, **3**, e1601659 (2017). Doi: <https://doi.org/10.1126/sciadv.1601659>
45. S. Mukhopadhyay, T. Thompson, J. Sakamoto, A. Huq, J. Wolfenstine, J. L. Allen, N. Bernstein, D. A. Stewart, and M. D. Johannes, Structure and Stoichiometry in Supervalent Doped Li₇La₃Zr₂O₁₂, *Chemistry of Materials*, **27**, 3658 (2015). Doi: <https://doi.org/10.1021/acs.chemmater.5b00362>